

# Simultaneous Imaging and Spectroscopy of the Solar Transition Zone

Charles C. Kankelborg<sup>1</sup>  
Jonathan Cirtain & Amy Winebarger<sup>2</sup>

August 19, 2013

<sup>1</sup>Department of Physics, Montana State University

<sup>2</sup>NASA Marshall Space Flight Center

## Abstract

The transition region of the solar atmosphere is the interface between the million-degree corona and the chromosphere. It is through this interface that mass and energy must flow to heat the corona and power the solar wind. Additionally, this region of the solar atmosphere is rich with dynamic events that are indicative of magnetic reconnection. Energy release in the atmosphere via magnetic reconnection is most clearly seen in transition region lines.

We propose to develop the EUV Snapshot Imaging Spectrograph (ESIS), a rocket borne next-generation imaging spectrograph, to observe the dynamical evolution of the solar atmosphere in the transition region O v 63.0 nm line, and in the corona with Mg x 62.5 nm. The new instrument will be integrated into an existing payload, alongside the successful Multi- Order Solar EUV Spectrograph (MOSES) instrument. MOSES is currently being refitted to observe the upper transition region and low corona in Ne VII 46.5 nm. When these two instruments fly together, we will observe the solar atmosphere over a large field of view at high cadence in three temperature regimes: 0.25 MK (O v), 0.5 MK (Ne VII), and 1 MK (Mg x).

For more than a century, our community has been peering at the Sun through a medieval arrow loop, the spectrographic slit. Acquiring an  $x, y, \lambda$  data cube requires rastering that slit, which takes a long time compared to the dynamics we are observing. Our next generation imaging spectrographs, ESIS and MOSES, obtain spectroscopic data over a wide field of view in every exposure. We will have comprehensive observational access to the physics of reconnection events, for the first time observing reconnection “from the inside out.” Moreover, we will trace the flow of energy between the transition region and the lowest reaches of the corona. We will thus elucidate the role the transition region plays in energizing the solar atmosphere.

We propose to launch the MOSES-ESIS payload from White Sands Missile Range in 2017. This investigation has strong synergy with orbital heliophysics missions. Our observations will be complementary to data from SDO/AIA, IRIS, and others.

## Contents

<b>1</b>	<b>Scientific Motivation</b>	<b>1</b>
1.1	Reconnection Events . . . . .	1
1.2	Energy Transport . . . . .	4
1.3	Science Requirements . . . . .	5
<b>2</b>	<b>Technical Approach</b>	<b>6</b>
2.1	Instrument . . . . .	6
2.1.1	Optics . . . . .	6
2.1.2	Cameras . . . . .	9
2.1.3	Avionics . . . . .	10
2.1.4	Data Handling . . . . .	10
2.1.5	MOSES electronics and ESIS accommodation . . . . .	10
2.1.6	Mechanical . . . . .	11
2.1.7	Design suited to inversion. . . . .	11
2.1.8	Mission Profile . . . . .	12
2.2	Calibration . . . . .	12
2.3	Coordinated Observations . . . . .	14
2.4	Data Analysis . . . . .	14
<b>3</b>	<b>Scientific Impact</b>	<b>17</b>
3.1	Impact of Proposed Work . . . . .	17
3.2	Educational Impact . . . . .	17
<b>4</b>	<b>Relevance to NASA Objectives and Programs</b>	<b>18</b>
<b>5</b>	<b>Plan of Work</b>	<b>19</b>
5.1	Roles & Responsibilities . . . . .	19
	<b>References</b>	<b>23</b>

# 1 Scientific Motivation

The solar transition region (TR) is the solar plasma that exists at temperatures between the dense, cool (20,000 K) solar chromosphere and the tenuous, million-degree corona. Initially, the transition region was viewed as simply the thin interface region between the chromosphere and corona, where the temperature of the plasma dramatically increased two orders of magnitude over tens of kilometers. Though undoubtedly this type of transition region exists in hot coronal loops, the concept of the transition region has been expanded over the last twenty years to include a dynamic and complicated three-dimensional geometry. It is in the low transition region where the magnetic pressure begins to dominate the plasma pressure. The transition region is rife with magnetically driven phenomena such as explosive events (Dere et al.(1991)Dere, Bartoe, Brueckner, Ewing, & Lund) and microflares (Gontikakis & Winebarger(2012)) and associated flows of 100+ km/s.

Investigations of the TR to date are severely limited by our observational capabilities. It is currently not possible to build an imager in this region with a narrow enough passband to capture the emission lines and limit the contribution of the continuum and other lines. Instead, slit spectrometers are used to study the transition region. Two-dimensional images must be built by rastering, which takes much longer than the timescales of TR phenomena.

We propose to launch the next generation EUV spectrometers to investigate the transition region of the Sun. A new instrument, EUV Snapshot Imaging Spectrograph (ESIS), will observe the transition region and low corona in the O v 63.0 nm and Mg x 62.5 and 61.0 nm spectral lines. ESIS will be conjoined to the existing and successful Multi-Order Solar EUV Spectrograph (MOSES) instrument. MOSES is currently being refitted to observe the upper transition region and low corona in Ne VII 46.5 nm. The joint MOSES-ESIS payload will be launched from White Sand Missile Range in 2017.

The ESIS/MOSES mission will address two overarching science goals:

1. Observe reconnection directly, “from the inside out.”
2. Map the transfer of energy through the transition region, emphasizing MHD waves.

To achieve goal 1, we will use ESIS and MOSES to map flows as a function of time and space in multiple transition region reconnection events in O v and Ne VII. In support of goal 2, we will cross-correlate the evolution at 250,000 K (O v) with that at 500,000 K (Ne VII) and 1 MK (Mg x) to map the vertical transport of energy over a wide field of view.

## 1.1 Reconnection Events

Solar flares, an essential ingredient of space weather and a major focus of heliospheric physics research, are believed to be driven by magnetic reconnection. However, studies of coronal reconnection events have been limited to the region outside the reconnection site, diagnosing reconnection “from the outside in”. For example, outflows far from the reconnection region are observed as supra-arcade downflows (McKenzie(2000); Savage et al.(2012)Savage, McKenzie, & Reeves). The rate of reconnection is inferred from magnetic flux overrun by flare ribbons (Qiu et al.(2004)Qiu, Wang, Cheng, & Gary; Asai et al.(2004)Asai, Yokoyama, Shimojo, Masuda, Kurokawa, & Shibata; Miklenic et al.(2007)Miklenic, Veronig, Vrsnak, & Hanslmeier). With compact flares, the overall topology of the event and kinematics of the emerging jets can be investigated (Masuda(1994);

Shibata et al.(1995)Shibata, Masuda, Shimojo, Hara, Yokoyama, Tsuneta, Kosugi, & Ogawara; Ohyama & Shibata(1998)). In rare instances, objects hypothesized to be plasmoids propagating along a current sheet have been observed (Savage et al.(2010)Savage, McKenzie, Reeves, Forbes, & Longcope; Takasao et al.(2012)Takasao, Asai, Isobe, & Shibata). The coronal reconnection region, however, is usually not observed for two reasons. First, the filling of the field lines with emitting plasma occurs via chromospheric evaporation driven by the reconnection energy release. The flaring loop therefore has low emission measure until well after it has been reconnected. Ironically, this is especially true of the largest flares, in which the reconnection is inferred to occur very high above the photosphere. Second, the corona has a large emitting volume compared to the reconnection site itself, so that there is emitting material on the line of sight before and behind the small reconnection region. To our knowledge, there are no reports to date of a slit spectrograph pointing in the right place at the right time to diagnose a flare reconnection region.

In the transition region, the densities are an order of magnitude higher than the corona and the radiative loss function is also higher, resulting in more observable radiation, so the reconnection region may be directly observed. Indeed, placing a spectrograph slit at random on the sun at any given time is likely to result in the observation of an explosive event. Explosive events (EEs) are compact line broadenings of order 100 km/s observed in transition region lines. They are extremely common in the solar transition region (TR), with up to 30,000 occurring at any one time on the sun (Dere, 1994). Despite their frequent association with magnetic elements in the network lanes, the presence of supersonic flows near the Alfvén speed, and other evidence of magnetic reconnection (e.g., Dere et al.(1991)Dere, Bartoe, Brueckner, Ewing, & Lund; Innes et al.(1997b)Innes, Inhester, Axford, & Wilhelm), their nature remains elusive. Muglach (2008) found many explosive events without evident magnetic counterparts. A range of morphologies have been posited, including simple oppositely-directed jets (Innes et al.(1997a)Innes, Inhester, Axford, & Wilhelm; Innes & Teriaca(2013)), spinning spicules (Curdtt & Tian(2011); Curdtt et al.(2012)Curdtt, Tian, & Kamio), and small eruptive events (Innes & Teriaca(2013)); however the 1D nature of the spectrograph slit makes it difficult to ascertain.

Transition region explosive events provide a unique opportunity to study magnetic reconnection in a solar context, but that potential has not yet been realized due to the limits of our observational tools. Spectrographs are limited to the portion of the event that happens to fall on the slit. Our proposal provides a way forward using a methodology proven by the first launch of the MOSES rocket instrument.

Using the MOSES rocket instrument, Fox et al.(2010)Fox, Kankelborg, & Thomas discovered a pinwheel-like structure in a He II explosive event, with a oppositely directed jets that were disjoint but tangent to a broadened core. MDI magnetograms show that the event occurred above a converging magnetic bipole. Numerical inversion of the same data, shown in figure 1, provides greater detail, showing a complex flow pattern within the event (Fox(2011); Fox & Kankelborg(2012)). The velocities are supersonic with respect to the He II plasma, implicating the conversion of magnetic to kinetic energy. The offset, misaligned jets were not anticipated in any model, and would not likely be revealed by a slit spectrograph. The distinct core structure, with line broadening and a complex pattern of flows, may be the first spectroscopic measurement of velocities associated with a tearing mode instability (Furth et al.(1963)Furth, Killeen, & Rosenbluth; Bárta et al.(2008)Bárta, Vršnak, & Karlický; Bhattacharjee et al.(2009)Bhattacharjee, Huang, Yang, & Rogers). Figure 2 is a simple 2D illustration of a current sheet (a) evolving to a tearing mode reconnection (b). We

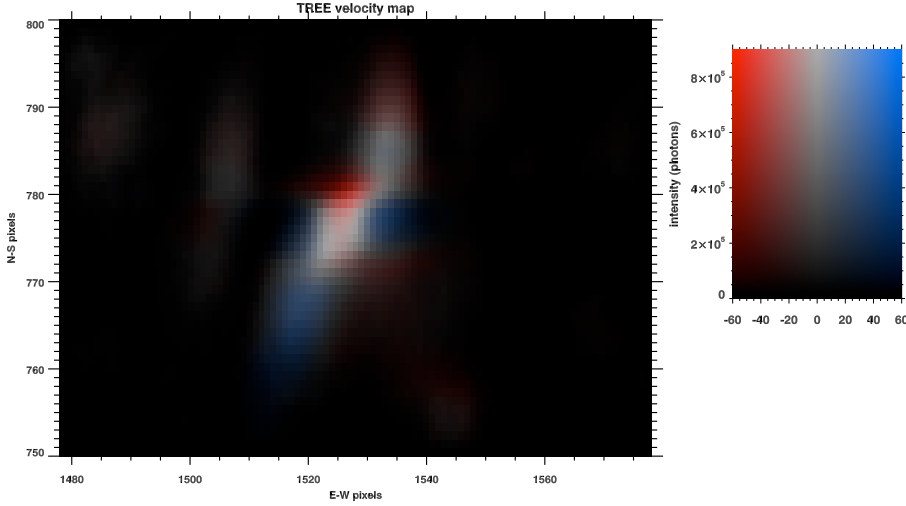


Figure 1: Dopplergram of a transition region explosive event, computed by inversion of He II images from the MOSES rocket instrument. The horizontal scale in the color legend is line of sight velocity in km/s. The inversion also shows significant broadening in the event core.

have illustrated only the fastest flows (those accelerated by magnetic tension), with blue (upward) and red (downward) arrows, emerging from the multiple reconnection sites along the current sheet. Only the flows at the ends of the current sheet in figure 2 b are immediately able to leave the core as jets. The other flows are accelerated into each other by equal and opposite forces, with no net momentum imparted to the resulting plasmoids. The resulting signature would be a core with multiple, oppositely-directed flows and two emerging jets. We hypothesize that Fox's He II event, with its two expanding jets and compact, turbulent core, represents a tearing mode reconnection in an asymmetric, 3D configuration.

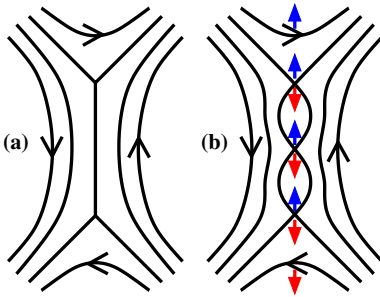


Figure 2: (a) A current ribbon between oppositely directed magnetic fields. To increase the generality of this picture, one might imagine a guide field, or a curved ribbon following a magnetic separator in 3D. (b) Tearing mode reconnection initiates at multiple points along and across the current ribbon, resulting in turbulent flows. The blue and red arrows mark flows accelerated to an appreciable fraction of the Alfvén velocity by magnetic tension.

The extension of the next-generation spectrographic technique pioneered by MOSES to additional transition region lines (Ne VII with MOSES-II, and O V with ESIS) will allow us to observe many more events, and to map the flows within and around simultaneously at temperatures of 0.5 MK (Ne VII) and 0.25 MK (O V). We will literally diagnose reconnection from the inside out. Explosive events are sufficiently common to provide a statistically meaningful sample in a 5-minute rocket flight. (For reasons that are unclear, explosive events are almost unknown in He II. The observation by Fox et al.(2010)Fox, Kankelborg, & Thomas doubtless owes much to the large MOSES field of view. Explosive events should be well represented in the O V line which we have chosen for ESIS (Moses et al.(1994)Moses, Cook, Bartoe, Brueckner, Dere, Webb, Davis, Harvey, Recely, Martin, & Zirin).)

## 1.2 Energy Transport

Tracking the mass and energy flow from throughout the solar atmosphere is a long-standing goal in solar physics and the primary goal of the Solar-C mission. Bulk mass flow is evidenced by Doppler shifts in spectral line profiles or skewness in spectral lines. Additional symptoms of energy flow are the non-thermal broadening of spectral lines. This is a broad topic, and our proposed instrumentation can address it in many ways. In this section, we will focus on a single application, searching for the sources of MHD waves that heat the corona and drive the solar wind.

Alfvén waves in coronal holes are observed to carry  $7e5 \text{ erg cm}^{-2} \text{ s}^{-1}$ , enough to energize the fast solar wind (Hahn et al.(2012)Hahn, Landi, & Savin; Hahn & Savin(2013)). The source and frequency spectrum of these waves is unknown. However, we hypothesize that MHD waves are similarly ubiquitous in quiet sun and active regions, and play an important role in the energization of the quiescent corona.

Transition region linewidth maps obtained with ESIS will be relatively close to any chromospheric sources, but will be insensitive to waves that are merely trapped in the chromosphere. The concentration of nonthermal energy mapped by ESIS in O V will therefore serve as an indicator of source density. We may arrive at a lower limit on the nonthermal velocity to be observed as follows. Since the waves are weakly damped and the solar wind velocity is much less than the Alfvén speed at altitudes below about  $R \leq 1.15R_{\odot}$ , the wave amplitude depends only weakly on density,  $v_{nt} \propto n_e^{-1/4}$  (Hahn & Savin(2013), and references therein). Assuming pressure balance between the low corona and transition zone, we may infer nonthermal velocities in the transition region by scaling according to the temperature drop,  $v_{nt} \propto T_e^{1/4}$ . The measured nonthermal velocity of 24 km/s for Si VIII near the limb (Doyle et al.(1998)Doyle, Banerjee, & Perez) should correspond to velocities of 21 km/s in Ne VII and 18 km/s in O V, which we assume are formed near their ion equilibrium temperatures in the TR.

There is a range of possible sources for MHD waves in the solar atmosphere, from spicules (typical width 250 km) to granules (1 Mm) and larger. The ESIS plate scale is .487 Mm per pixel, which will allow us to access a significant portion of the relevant range of scales. What we require, however, is not to resolve the sources but to localize them for comparison with other solar imagery. Transition region observations should allow us to pinpoint the locations of sources that are spaced, say,  $> 2 \text{ Mm}$  apart. The resulting nonthermal widths for localized sources will be significantly higher than the  $\sim 20 \text{ km/s}$  mean derived above. Our own data will show us whether these sources are associated with explosive events, macrospicules, etc. Comparison with a wider selection of ground and space based imagery will allow us to determine whether converging or emerging magnetic bipoles, type II spicules, spicule bushes, or other sources beneath the TR are associated with the source density.

**Transition region seismology.** In a 5-min. rocket flight, we will see change at small scales over the entire field of view. The disturbances we see will take the form of doppler shifts, intensity fluctuations, motions in the skyplane, and nonthermal line broadenings associated with frequencies too fast for our 3-10s cadence. The transverse motions can be mapped automatically by local correlation tracking (Welsch et al.(2007)Welsch, Abbett, DeRosa, Fisher, Georgoulis, Kusano, Longcope, Ravindra, & Schuck), which was designed to track photospheric flows, but has recently been applied to EUV flare data (McKenzie(2013)). We will map all these quantities as a function of time in O V, Ne VII, and Mg X. The quantities mapped in a given channel can be fourier-transformed in space and time (with 30-100 ESIS time series points in the rocket flight) to

give a  $k - \omega$  diagram. However, we are most interested in vertical propagation. By cross-correlating the vector velocities and intensities between any two ions as a function of time delay, we expect, at minimum, to distinguish upward and downward propagation of disturbances in the transition region. Since we have access to both transverse (sky plane) and longitudinal (Doppler) motion, a variety of MHD modes can be distinguished. Ideally, we hope to develop the method sufficiently to derive upward and downward fluxes of wave energy on a per-mode basis.

### 1.3 Science Requirements

The strategy of this investigation focuses on two science targets: (1) Reconnection in explosive events, (2) Transport of mass & energy through the transition region. The latter may take many forms, from MHD waves of various modes to EUV jets or macrospicules. Table 1 lays out important temporal, spatial, and velocity scales derived primarily from the references listed in the previous section.

Table 1: Parameters for some phenomena relevant to the ESIS/MOSES science goals.

Objective	Length (Mm)	Timescale (s)	$v_{nt}$ (km/s)	location
Explosive events	1-6	60-90	100-400	QS & AR
MHD wave sources	0.5+	60-300	18	QS, CH
Jets, Macrospicules	3-20	300+	50-150	QS, AR, limb

ESIS must obtain simultaneous intensity, doppler shift and line width images of the O v 63 nm line in the solar transition region at rapid cadence. We accomplished similar measurements in He II with MOSES by using a single, large grating to form images at three spectral orders,  $m = -1, 0, +1$  (Kankelborg & Thomas(2001); Fox et al.(2003)Fox, Kankelborg, & Metcalf; Fox et al.(2010)Fox, Kankelborg, & Thomas). The differing magnitude and direction of dispersion among these three images makes it possible to derive line shifts and widths anywhere in a large field of view (§2.4).

By merging the considerations in table 1 to the tightest constraints in each category, we arrive at the ESIS instrument requirements in table 2.

Table 2: ESIS Instrument Requirements.

Parameter	Requirement	Design	Science Driver
Spectral line choice	O v	O v & Mg x	Explosive events
Spectral resolution	18 km/s line width	$\ll 16$ km/s	MHD waves
Spatial resolution	2'' (1.5 Mm)	1.5'' (1.1 Mm)	Explosive events
Count rate	30 phot/s in CH	108 phot/s	MHD waves in CH
Cadence	30 s	$< 10$ s	Explosive events
Observing time	$> 180$ s	$\sim 300$ s	MHD waves
FOV	$10' \times 10'$	$12' \times 12'$	Span QS, AR, limb



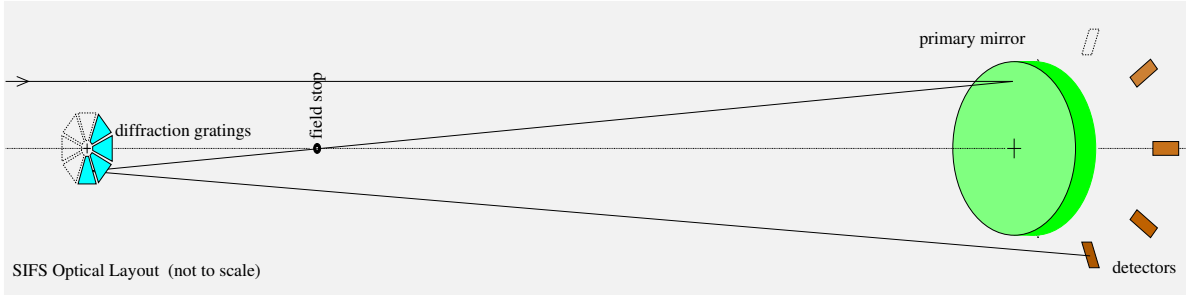


Figure 3: The ESIS instrument is a pseudo-Gregorian design. The field of view is defined by a field stop at prime focus. After the field stop, the light falls on multiple concave diffraction gratings, each associated with a particular CCD sensor. Four channels are populated for the first flight.

## 2 Technical Approach

### 2.1 Instrument

The EUV Snapshot Imaging Spectrograph (ESIS) is a next-generation imaging spectrograph that obtains line intensities, Doppler shifts, and widths in a single snapshot over a 2D field of view. The design presented in this section meets all the science requirements set forth in § 1.3.

#### 2.1.1 Optics

Like our original MOSES instrument (Kankelborg & Thomas(2001); Fox et al.(2010)Fox, Kankelborg, & Thomas; Fox(2011)), this is a two-reflection design. It is also a multiple projection slitless spectrograph like MOSES, but the similarities end there. The new instrument has a modified Gregorian layout, as illustrated in figure 3. Light entering the telescope is brought to focus by the parabolic primary mirror at an octagonal field stop. From the field stop, light is re-imaged to a CCD by one of four concave gratings, each of them oriented so that the symmetry axis of the primary lies in the dispersion plane. The table below lists preliminary design information for the optics.

ESIS uses four identical, small concave spherical gratings, optimized to work in first order. These are aberration corrected (varied line space) gratings (Poletto & Thomas(2004)). They are all replicas of a single master grating. This is a different strategy from the large MOSES and MOSES-II gratings, which had a very tight specification for the groove depth to achieve the required distribution of intensity in the central three diffraction orders. MOSES is an elegant design, but it suffers astigmatism due to the compromise of forming three widely separated images with a single optic. The optical raytrace of ESIS (figure 4) shows spot sizes that fit well within a pixel.

ESIS has a modest magnification, and its alignment tolerances are therefore easily manageable.

**Coatings & Filters.**

The primary mirror and diffraction gratings will be coated by Dr. David Windt (Reflective X-Ray Optics LLC) with a Si/Gd multilayer optimized for 63 nm. The peak reflectivity of this coating is 30%. Figure 5 shows the total throughput of two reflections, based on actual measurements (Windt et al.(2009)Windt, Bellotti, Kjornrattanawanich, & Seely). This material set achieves its

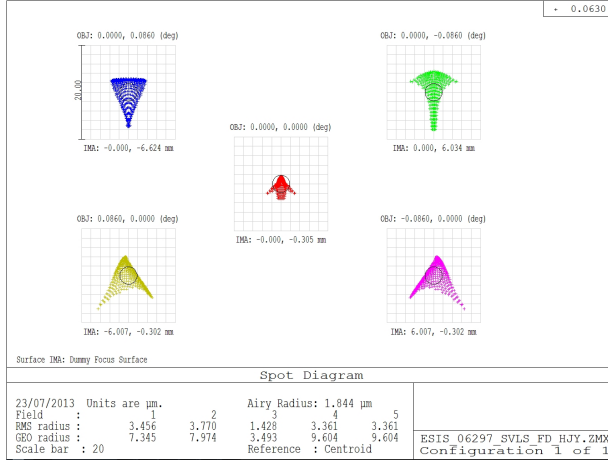


Figure 4: Optical performance of *ESIS*, illustrated by spot diagrams at the center and edges of the detector. Imaging performance will be limited by the  $15\ \mu\text{m}$  pixel size.

full reflectivity and selectivity with only 4 layer pairs. Since the coating is thinner than many EUV multilayers, the effects of stress on the optics are significantly reduced. Tungsten interlayers will be used to stabilize the coating against diffusion, as described by Windt et al. We note that the bandpass of *ESIS* is determined by the combination of the field stop and grating, as illustrated in figure 6.

Luxél thin film Al filters 100 nm thick will be used to shield each CCD from visible light. The thin metallic film is supported by a 70 lpi Ni mesh, with 82% transmission. Our approach is modeled after the MOSES design, which has each CCD in a light tight box with a labyrinthine evacuation vent and an Al filter. The distance from filter to CCD is optimized to zero the shadow of the mesh on the detector. This is accomplished by choosing a position such that the light incident on a detector pixel intercepts a large, integral number of mesh cells. The MOSES flight data and inversion residuals show no detectable signature of the mesh.

**Field Stop.** Since we use a field stop in this new configuration, we are able to eliminate edge effects which degraded line profile recovery near the edges of the MOSES FOV. The field stop also helps to separate wavelengths that are off-band. Figure 5 shows the *ESIS* field of view relative to that of MOSES on the solar disk. The pointing in the figure is arbitrary.

#### ESIS Optical Design Parameters

Primary	Parabolic, $D = 175\ \text{mm}$ Focal length 1.0 m Si/Gd multilayer, $\lambda 63\ \text{nm}$ Transparent vis/IR
Field Stop	12.2 arcmin Octagonal
Gratings (4)	Spherical varied line space (replicas of one custom master) Trapezoidal, $23 \times 21\ \text{mm}$ Groove spacing $d = 0.3358\ \mu\text{m}$ Magnification $M=4$
Filters (4)	Si/Gd multilayer, $\lambda 63\ \text{nm}$ 38 mm thin film 100 nm Al
Detectors (4)	82% open Ni mesh E2V CCD230-42 active area $1032 \times 2048$ pixel size $15\ \mu\text{m}$ QE 94% (measured, $\lambda 63\ \text{nm}$ )
Plate scale	0.77 arc sec / pixel $25\ \text{m}\text{\AA}$ (5 km/s) per pixel
Resolution	1.55 arc sec (Nyquist limited)

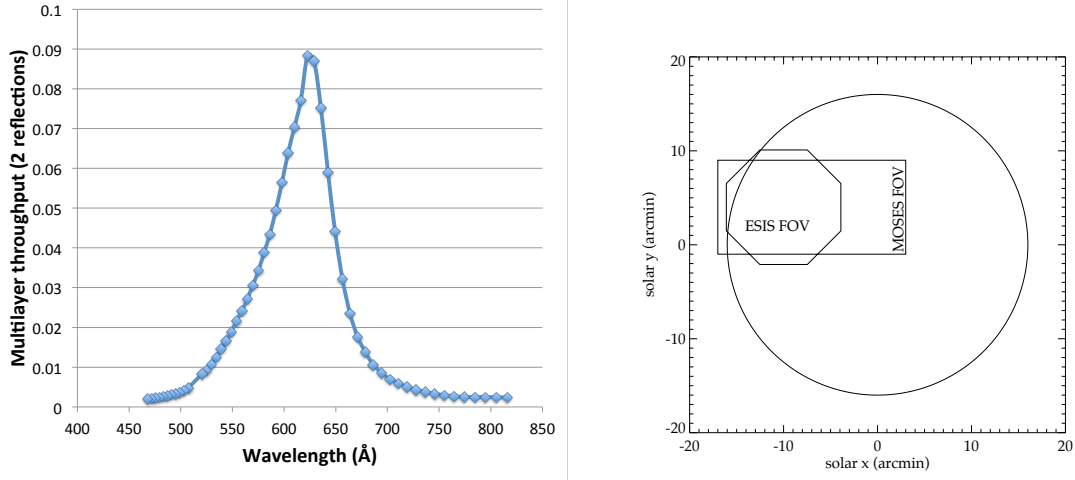


Figure 5: (Left:) Measured throughput of Si/Gd multilayer coating, squared for two reflections. (Right:) Size of the ESIS and MOSES fields of view, superimposed on the solar disk at an arbitrary pointing.

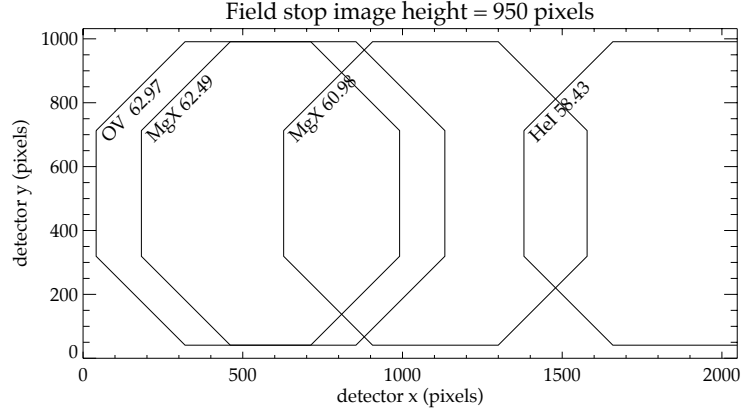


Figure 6: Areas occupied by strong spectral lines on the ESIS detectors. The plot axes are sized exactly to the CCD active area.

**Dispersion.** Figure 6 shows where images of each strong spectral line will fall on the ESIS detectors. He I is completely disentangled from our target lines of O v 62.97 nm and Mg x 62.49 nm. There is an 'extra' Mg x line, at 60.98 nm. The 60.98 nm line is consistently twice as strong as the 62.5 nm line. These lines are not density sensitive. They are essentially redundant, but having most of the 60.98 nm line outside the He I image will make it easier to separate O v and Mg x without crosstalk. The relatively high dispersion of ESIS (compared to MOSES)

**Sensitivity & Cadence.** Estimated count rates (below) are sufficient to obtain high quality inversions with 3-10 s exposures, even in coronal holes. With only 1.1 s readout time and zero latency due to shutterless operation, ESIS will achieve cadence limited only by exposure time. Unlike a rastering slit spectrograph, ESIS exposes with 100% duty cycle, obtaining 30-100 images in a 5-minute rocket flight.

Count rates (photons per pixel per second) for ESIS lines in coronal hole (CH), quiet sun (QS),

and active region (AR). The sources are (Vernazza & Reeves(1978)), and the CDS data cube used in the example inversion (2.4).

solar context	count rate		source
	O v 63 nm	Mg x 62.5 nm	
QS	127	19	V&R
CH	108	1	V&R
AR	386	151	V&R
AR	197	91	CDS

**Upgrade potential.** ESIS has 4 channels, offering more spectral information than the 3-channel MOSES design. As will be apparent from figure 3, each of our four detectors is illuminated by 1/8 sector of the primary. The instrument is half populated, leaving room for 4 more gratings and detectors (2 within the current payload optical bench structure). This strategy allows us to demonstrate the power of the new instrument design, while proposing at a cost that is within range for the LCAS program. Once we have demonstrated successful recovery of line profile information in our first flight, we will propose an upgrade to either 6 or 8 detectors. With more channels, the instrument will gather enough information to determine higher moments of the line profiles.

### 2.1.2 Cameras

The ESIS cameras are based on the prototype CCD camera designed by MSFC specifically for use on solar space flight experiments. The prototype camera is equipped with a single readout channel, and has demonstrated a readout noise of 6.9 electrons rms at 500 kpixel/sec readout speed. A flight camera with 2 readout channels is currently under development, and will be flown on a sounding rocket experiment (Chromospheric Lyman Alpha Spectro-Polarimeter: CLASP) in 2015. The CLASP cameras will demonstrate operation of 3 cameras from a single data system, and synchronized (lock-step) image acquisition in frame-transfer mode using an external trigger signal. The ESIS camera will be based on the CLASP camera but increases the number of readout channels to 4, each with a dedicated 16-bit A/D converter. The design of each readout channel will remain unchanged to insure the same low noise performance. The CCD230-42 will be operated in a split frame transfer mode using 4 readout amplifiers, using the central  $2048 \times 1032$  pixels for imaging and the two outer  $2048 \times 516$  pixel regions for storage. When the camera receives the trigger signal, it transfers the image from the imaging region to the storage regions and starts image readout; the digitized data are sent to the Data Acquisition and Storage system (DACS) through a SpaceWire interface immediately, one line at a time. The frame transfer takes only 20 ms, and readout takes 1.1 seconds, which represents the maximum cadence of this camera. Because the imaging region is continuously illuminated, the action of frame transfer (transferring the image from the imaging region to the storage regions) also starts the next exposure without delay. Thus the exposure time is controlled by the time period between triggers. All 4 cameras are triggered by a single trigger pulse generator to an accuracy of  $< 10$  ms. The camera enclosure will be custom designed for ESIS due to the unique packaging requirements for this experiment. The front part of the camera is a metal CCD block which holds the CCD in place and equalizes the temperature across the CCD. The CCD blocks of all cameras will be connected to a central cold block through heat straps; the cold block will be cooled by LN2 flow from outside the payload until just before launch. The LN2 flow will be controlled to ensure that all the cameras are above survival temperature and below the

target temperature of -30C to insure a negligible dark current level.

### 2.1.3 Avionics

The ESIS DACS will be based on the Hi-C electronics. The Hi-C electronics successfully flew in August 2012. The electronics are based on Military Off-The-Shelf (MOTS) hardware and custom designed components. The DACS is a 5-slot 3U Compact PCI conduction cooled system using an AiTech Core7 single board computer. The data system also includes conduction cooled MOTS high speed serial card, 16 Gbytes solid state storage card, two MOTS 3 channel Spacewire cards, and custom design telemetry output card. The Core7 SBC is a quad core Pentium operating at 2.0 GHz with 2Gbytes of memory. The operating temperature range for the data system is -40 to +85 C. Custom DC/DC converters are used for secondary voltages required by other electronic components. The use of custom designed converters allowed additional ripple filtering for low noise. The operating system for the flight data system is Linux Fedora Core 19. The ESIS Ground Support Equipment (GSE) used for ESIS experiment operations is based around a National Instruments PXI system mounting in a mobile shipping case. The GSE operation system is Linux SUSE 11.3. The GSE provides remote operational control for the ESIS experiment. The GSE can either interface to the White Sands Missile Range (WSMR) telemetry decom system or directly to the ESIS instrument as a unit tester. The GSE displays the ESIS instrument health and status, target images and science images that are telemetered. The GSE also provides a checkout control for ground operations. The GSE software is mission configurable via XML files.

### 2.1.4 Data Handling

The DACS uses a standard file system, and the data from the 4 cameras are saved as individual FITS files along with time tag, exposure time and other metadata stored in the header. A separate process selects a partial set of data for downlink, formats the data into telemetry frames and sends them to the telemetry through the parallel I/O interface at 10 Mbit/s. Approximately 20 sets of 4 full-resolution images can be downlinked during flight, enough to satisfy minimum science requirements even in case of loss of payload.

### 2.1.5 MOSES electronics and ESIS accommodation

During both flights (MOSES-II in year 1, followed by ESIS/MOSES in year 4), the MOSES payload will use its existing electronics system. For the flight with ESIS, the MOSES data will be desired but not required for minimum mission success. Its high speed telemetry interface will be removed and its science data will be stored onboard only. Like ESIS, MOSES uses liquid nitrogen at the rail. Both can be served from the same dewar, but ESIS EGSE will control its own supply. The

Table 3: ESIS Mass Estimates (kg)

Optics	Primary	1.6
	Gratings	0.1
	Filters	0.1
Mounts	Primary	1.6
	Gratings	0.3
Electronics	Avionics	15.0
	Cameras	3.4
Subtotal	(CBE)	22.3
Margin	(25%)	5.6
TOTAL	w/margin	27.7

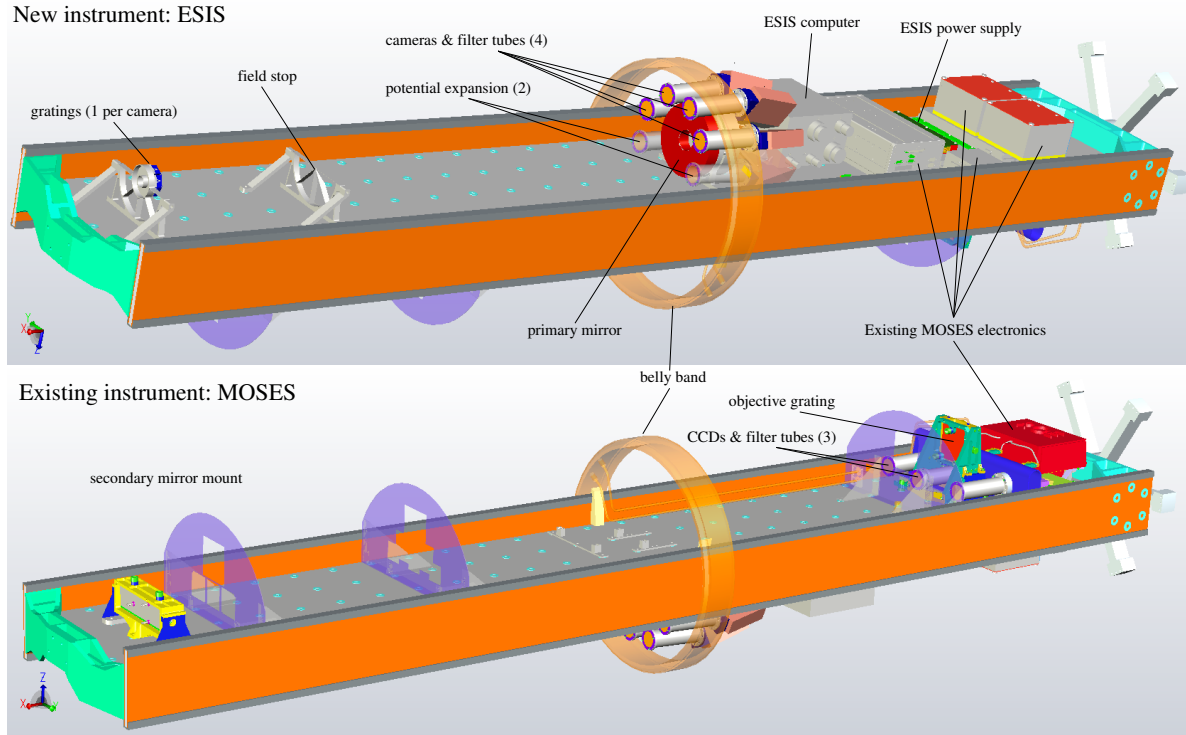


Figure 7: ESIS and MOSES mounted together in the payload experiment section. The belly band is included to illustrate the skin diameter in relation to the instruments.

two instruments will be fed via separate lines, requiring a second belly band port.

### 2.1.6 Mechanical

Our existing instrument, MOSES, is built on a composite optical table structure with a convenient, precisely coplanar array of threaded inserts with precision counterbores. There is ample room on the reverse side of this structure to accommodate the optics and electronics of the proposed new instrument, ESIS (7).

The existing MOSES experiment section weighs approximately 200 kg in its bulbous 22-in. skin section, 3 m in length. Following are preliminary mass estimates for the new hardware.

**Mechanisms** MOSES has a mechanical shutter, and there is a NASA-supplied standard shutter door on the payload section. ESIS will have no moving parts. Its cameras operate in shutterless mode.

### 2.1.7 Design suited to inversion.

We have taken advantage of our experience with MOSES to design ESIS for the ultimate recovery of spectral information from the data. The reconstruction of line profile information is a limited-

angle tomography problem (§ 2.4), so the fidelity is limited by the number of simultaneous images. MOSES formed 3 images using a single grating, which entails some aberrations in the outboard images, and cannot be practically extended to produce more. In its first incarnation, ESIS will have 4 detectors, but is designed so that it can be upgraded to 6-8. Each image is razor sharp because it is produced by its own (identical) aberration corrected grating.

Inversions of MOSES data to date have been affected by disparate point spread functions (PSFs) of the three MOSES channels, part intrinsic to the design, but part due to mount-related distortions. We anticipate improved performance for the 2014 flight, having diagnosed and relieved unintended stress in the mounts. ESIS has improved low-stress mount designs and much lower intrinsic aberration, allowing pixel-limited imaging.<sup>1</sup> ESIS also has nearly twice the dispersion of MOSES (16 km/s/pixel vs. 30 km/s/pixel), so that line profiles will be dominant over the ESIS PSF.

The final (and smallest) complication to MOSES inversion has been the discovery of a faint, continuum-like signal of coronal origins, similar in level to the nearby Si XI line. The source of these features is a combination of multiple, unidentified weak lines and EUV continuum within our instrument passband. Much of this light is collected from outside our intended field of view and superimposed on the He II images by the grating. ESIS is designed with an octagonal field stop that defines the field of view before the light is dispersed by the gratings. The high dispersion of ESIS works with the field stop to minimize the overlap of off-band light with our target lines at 62.5-63 nm.

### 2.1.8 Mission Profile

Both proposed launches (MOSES-II 2014 and ESIS-MOSES 2017) are solar pointed SPARCS flights from White Sands Missile Range. We will request cleanroom usage, liquid nitrogen at the rail, helicopter recovery, and other support that is typical of solar sounding rocket launches. As ESIS will be incorporated into the existing MOSES experiment section, only minimal machining support from Wallops Flight Facility (additional liquid nitrogen port and bulkhead electronic feedthroughs). The two experiments operate independently after they begin their exposure sequence from a timer signal generated within the telemetry section.

Data can be obtained above  $\sim 160$  km. We aim for approximately 250-300 s above this altitude.

## 2.2 Calibration

With both MOSES and ESIS, we have three motivations for calibration in vacuum:

1. Verify instrument function in EUV/FUV.
2. Characterize detectors.
3. Support estimates of flight exposure time (radiometry within a factor of 2).

Under a partial award received in the 2011 LCAS competition, we developed a calibration capability at MSU that will support the EUV characterization of MOSES-II. We summarize the MOSES

---

<sup>1</sup>We will have to be careful of aliasing due to the high performance of the ESIS optics. Aliasing can be prevented by an intentional, slight defocus of the telescope, so that the PSF slightly overfills the pixel.

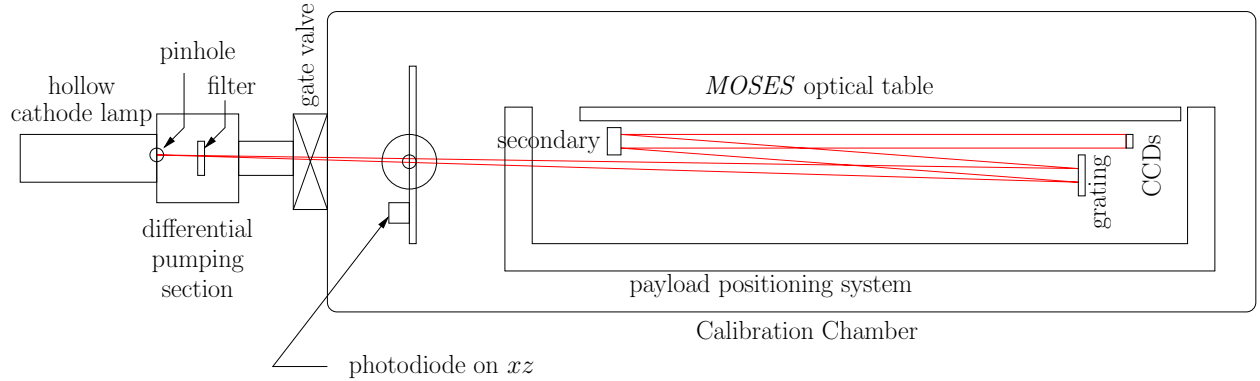


Figure 8: Block diagram of instrument calibration setup. Not to scale.

calibration approach here because it pertains to both MOSES and ESIS. The calibration system includes a vacuum chamber capable of holding the full payload at  $\sim 10^{-6}$  Torr, a manipulation system that moves the payload in pitch and yaw, an EUV hollow cathode light source, and a movable photodiode detector between the light source and the instrument (figure 8). This configuration of the calibration system (figure 8) allows detector flat fields, photon transfer curves, and end-to-end calibration to be obtained in one set of measurements.

A diverging, relatively uniform EUV beam emerges from a  $500\text{ }\mu\text{m}$  pinhole at the exit of our hollow cathode lamp. The incident beam shape has been characterized using a NIST-calibrated photodiode on an  $xz$  movement located between the gate valve leading from the differential pumping section and the payload support. Only the rays that are nearly parallel to the payload axis land on the CCDs. Each CCD is thus fully illuminated by a narrow bundle of rays that sample a small (approx.  $28 \times 14\text{ mm}$ ) part of the  $80\text{ mm}$  square aperture. Tip and tilt of the payload makes it possible to scan the beam over the aperture. We take a range of exposures at every position in this scan. The resulting set of images, taken as a function of tip, tilt, and exposure time, completely characterize both the CCD and the response of the optics. Since the instrument optical design is unvignetted, the interpretation of the data is straightforward. Nearly all of the calibration is done with flight filters removed, using instead an Al pre-filter installed near the pinhole. Since a single exposure samples a small area on each optic, the exposure is essentially a CCD flat field. Analysis of the noise in a range of exposures allows us to statistically infer the number of photons per DN. Each tip-tilt position samples a different part of the aperture, so that taken together they provide a map of any throughput nonuniformity in the optics, which can be compared against synchrotron data obtained after coating deposition. The flight filters are subsequently reinstalled and can be calibrated by an exposure sequence taken at a single payload position. In this configuration, we will see a sharp image of the filter mesh and can directly measure any filter nonuniformity. The full calibration procedure requires pumping down twice for each instrument.

For ESIS, we will remove the field stop to obtain unvignetted calibration measurements covering the entire detector. Either pure Ne or a Ne-He mixture will be used in the hollow cathode. The spectrum of light on the detector will be dominated by the strong Ne I  $62.68\text{ nm}$  line.



### 2.3 Coordinated Observations

The experience of our team is that a rocket launch provides an excellent occasion for coordinated observations. We will take full advantage of this opportunity by reaching out to the observing community, both ground and space based, of our plans and also inviting them to collaborate with our team as we analyze the rocket data.

Our proposal has emphasized the scientific goals of the ESIS+MOSES flight in 2017. However, in year 1 of the proposed investigation, MOSES-II will be launched to observe the upper transition region and lower corona in Ne VII. Our observations will be most meaningful alongside context data from both higher and lower in the atmosphere. We plan to request coordinated observations with IRIS and Hinode in 2014, and will take advantage of coronal imaging from SDO/AIA. The ESIS PI is a co-investigator on IRIS, and is intimately familiar with IRIS operations and data analysis. Spectra and slit jaw images from IRIS will help us understand how 500,000 K material couples both to the underlying chromosphere and lower TR. Our tentative program would be FUV very large dense rasters, 10 s exposures, with slit jaw images in C II and Si IV alternating, through the rocket launch window<sup>2</sup> Synoptic multi-band EUV imagery from the Atmospheric Imaging Assembly (Lemen et al.(2012)Lemen, Title, Akin, Boerner, Chou, Drake, Duncan, Edwards, Friedlaender, Heyman, Hurlburt, Katz, Kushner, Levay, Lindgren, Mathur, McFeaters, Mitchell, Rehse, Schrijver, Springer, Stern, Tarbell, Wuelser, Wolfson, Yanari, Bookbinder, Cheimets, Caldwell, Deluca, Gates, Golub, Park, Podgorski, Bush, Scherrer, Gummin, Smith, Auken, Jerram, Pool, Soufli, Windt, Beardsley, Clapp, Lang, & Waltham) onboard the Solar Dynamics Observatory (SDO/AIA), will provide image context at rapid cadence in the lower transition region and corona. Taken together, these observations will help us to infer both where and how transient outflows are initiated, and to follow the transport of matter and energy through the solar atmosphere.

Our first launch of ESIS, in year 4 of the program, targets reconnection and the associated flows and nonthermal widths in the solar transition region. Our experience with the year 1 launch will help us to refine our coordination plans for the ESIS flight. Naturally, we hope that IRIS and SDO will be in their extended missions. Should they be unavailable, our core science of reconnection in the transition zone and its coupling to the corona can be accomplished with the combination of ESIS (O V, Mg X) and MOSES (Ne VII). Ideally, we would like to correlate the events we observe with coronal imagery from SDO/AIA. IRIS provides the opposite boundary, so that we can better localize the initiation of events that supply mass and energy to the corona. Wherever the IRIS slit is placed within the MOSES field of view, we are likely to see one or two explosive events in C II and Si IV. Our tentative plan would be a fast sit-and-stare observation with slit jaw images alternating between C II and Si IV to provide the event morphologies. Hinode/SOT BFI images would be desirable if available (e.g., high cadence time-series (12 s) of the H $\alpha$  blue wing at -40 and -60 km/s).

### 2.4 Data Analysis

The images obtained with MOSES and ESIS are analogous to the “overlappograms” produced by S082A (Tousey et al.(1977)Tousey, Bartoe, Brueckner, & Purcell; Feldman(1987)), but with two key differences (Fox et al.(2003)Fox, Kankelborg, & Metcalf; Fox & Kankelborg(2009); Fox et al.(2010)Fox, Kankelborg, & Thomas):

<sup>2</sup>A 1-hr window is typical for launches from White Sands Missile Range, due to agreements with civil authorities.

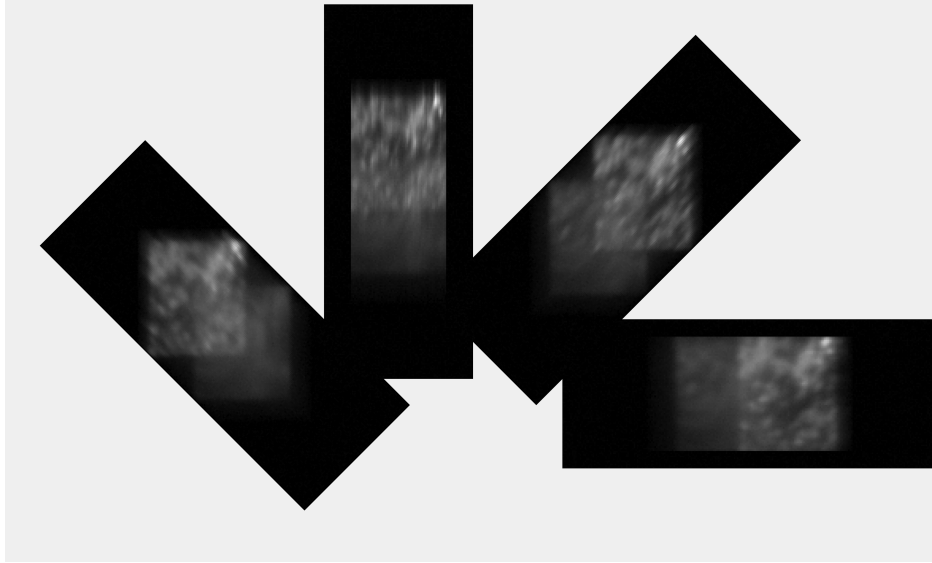


Figure 9: Four simulated ESIS images (4 large rectangles), projections at  $45^\circ$  intervals. Square root scaled. Dispersion is radially outward. Detector and shot noise have been applied to simulate a realistic 3 s exposure. Simulation based on a CDS raster. The two overlapping sub-images are Mg x (fainter) and O v (brighter). The CDS raster FOV bounds the images in a manner similar to the ESIS field stop, but is rectangular rather than octagonal.

1. We have multiple projections at different angles through position-wavelength space. This constrains the possible interpretations of the data, permitting certainty in the identification of flows and line broadenings.
2. Our coatings and optical geometry limit the instrument passband to a small number of lines, so that a relatively small number of images can be used to infer the spectrum.

There are at least two kinds of analysis that may be used to derive line profile information from this kind of data. The first is “parallax” analysis, in which the different projections are correlated to identify specific objects. Fox *et al.* (2010) derived unambiguous signatures of doppler shifts, line broadening, and two- component flows by the parallax method.

A more powerful mode of analysis is an automated inversion of the data to form a data cube, i.e. a spatially resolved spectrum as a function of  $(x, y, \lambda)$ , as discussed below. Our images are projections onto the sky  $(x, y)$  of a three-dimensional  $(x, y, \lambda)$  object. The inversion to recover the  $(x, y, \lambda)$  is a classic tomography problem (Kak & Slaney(1988)).

After testing a number of approaches (Fox et al.(2003)Fox, Kankelborg, & Metcalf), we have implemented a Smoothed Multiplicative Algebraic Reconstruction Technuqe (SMART). A similar recipe for reconstructing hyperspectral data was described by Okamoto (1991) . Our adaptation of this technique was first tested against synthetic data (Kankelborg & Fox(2004)) and then applied to the explosive event analyzed by Fox et al.(2010)Fox, Kankelborg, & Thomas (Fox(2011)). A dopplergram generated from the inversion is shown in figure 1. A paper concerning these results is in preparation (Fox & Kankelborg(2012)).

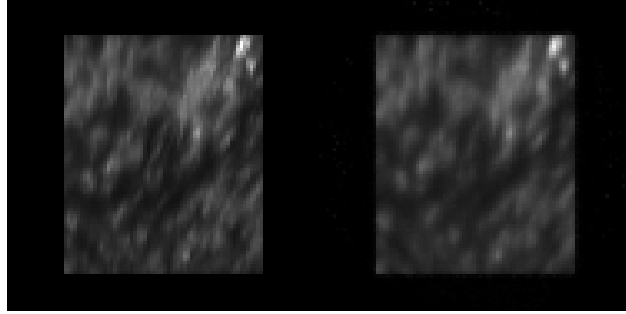


Figure 10: Line center image of O v, square root scaled. Left: Original CDS data cube. Right: SMART inversion from a single, simulated 3 s exposure.

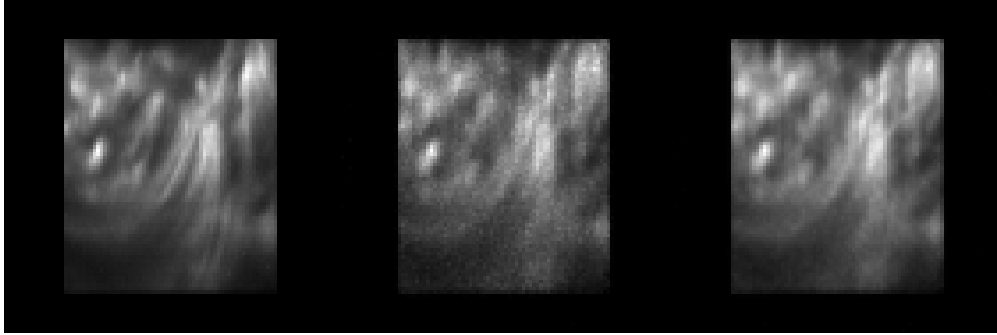


Figure 11: Line center image of Mg x, linearly scaled. Left: Original CDS data cube. Middle: SMART inversion from a single, simulated 3 s exposure. Right: SMART inversion integrated over the line profile to reduce noise.

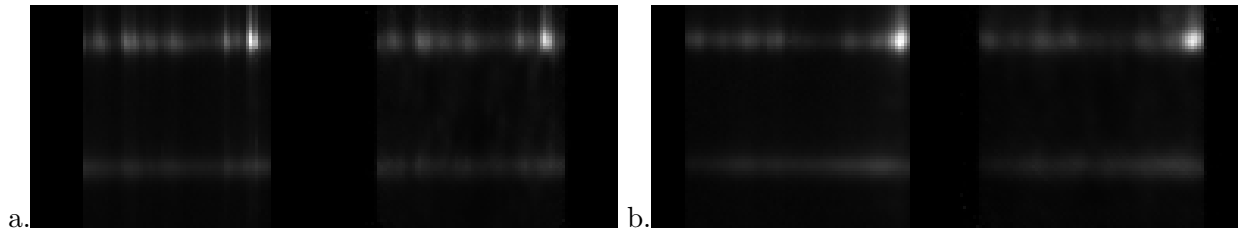


Figure 12: Spectra showing both O v (upper, with bright explosive event) and Mg x (lower). In each panel, the left side is the original CDS data cube, while the right side is the SMART reconstruction. Square root scaled. (a) From a horizontal cut of the data cube. (b) From a vertical cut. Both cuts go through the same bright explosive event.

We have prepared an example of the SMART algorithm as applied to ESIS. As a proxy for the Sun, we have used a SOHO/Coronal Diagnostic Spectrometer (CDS) (Harrison et al.(1996)Harrison, Kent, Sawyer, Hollandt, Kuhne, Paustian, Wende, & Huber) raster from a weak active region,

containing both the O v 63 nm and Mg x 62.5 nm lines. The Mg x 61 nm line is not included, however we expect the presence of this line to improve our results. Our simulation includes measurement-based camera noise, and shot noise consistent with a 3 s exposure. Figure 9 shows the appearance of the ESIS data, with the images oriented at four different angles as the detectors will be. For this simulation, we let the field stop be rectangular since it allows us to use all of the CDS raster, including an explosive event (bright point at the upper-right corner of the FOV).<sup>3</sup> The dispersion is radially outward, parallel to the long edge of each detector. The SMART inversion of this data took only 27 seconds in IDL on a laptop with a 2.7 GHz Intel Core i7. We recovered accurate line intensity maps for both O v (figure 10) and Mg x (figure 11). The O v image has extremely high contrast, so has been square root scaled to bring out faint features. This is a very high quality reconstruction of the line center, requiring less than 600 counts per pixel. Understandably, the Mg x line center image shows some noise. This line had only 273 counts per pixel in each ESIS image, and is somewhat overshadowed by the stronger line. As a rule of thumb, 300 counts/pixel is a typical lower limit for image formation, so the reconstruction quality in this example turn out to be limited by the short exposure we chose, rather than by the intrinsic difficulty of the inversion problem. The right panel of figure 11 demonstrates that integrating the image over the line profile reduces the noise considerably. Most importantly, line shifts and broadenings characteristic of the explosive event in O v are recovered (figure 12). Thus, with ESIS, we do not need to decide where to point a slit. The spectrum is recovered throughout the 2D field of view.

### 3 Scientific Impact

#### 3.1 Impact of Proposed Work

In § 1, we pointed out the variety of dynamical phenomena accessible to simultaneous imaging and spectroscopy in the transition region between the solar chromosphere and corona. The O v line is an excellent window into the dynamics of this interface. What ESIS adds to the work that has been accomplished to date is a simultaneous, rapid cadence, 2D map of doppler shifts and line widths. With these, we expect to characterize the evolution of the MHD instability that leads to the conversion of magnetic to kinetic energy in the transition region. The early evolution of flares at the moment of reconnection has been inaccessible in the corona, but we can observe the analogous process in the transition region with ESIS at a cadence fast enough to resolve the dynamics.

Moreover, ESIS is a potential precursor to future orbital instruments. It is a compact and lightweight design, and its optical design is capable of being pushed to much higher resolution. An instrument of this type with a TRACE-sized aperture could achieve sub-arcsecond resolution at very rapid cadence. The design is inherently versatile, as it may be targeted to any narrow region of spectrum in the EUV or FUV. Its bandpass can be defined by the grating and field stop if narrow band coatings are not available at a given wavelength.

#### 3.2 Educational Impact

Graduate and undergraduate education are a cornerstone of the MSU rocket program, and this emphasis will continue in ESIS development, launch, and scientific analysis.

---

<sup>3</sup>The shape is inconsequential to the inversion, so long as its image falls wholly on the detector in both spectral lines.

Currently there are four graduate students working on the MOSES program. All four are involved in both data analysis and hands-on hardware experience with the rocket payload. Each has written portions of a code we are currently using for inversion of MOSES data (§ 2.4). Hans Courier performed optical design simulations to support the development of this proposal. He is analyzing MOSES data to characterize waves and flows in the transition region, and in the course of this work recently happened upon a new approach to the analysis of MOSES data. He uses local correlation tracking to characterize the differences in image intensity distribution among the multiple spectral orders, leading to direct estimates of doppler shift and line width that are insensitive to the differing PSFs at the three focal planes (Courier & Kankelborg(2013)). Thomas Rust has developed our optical testing procedures and led the effort to calibrate our detectors. He has recently developed an algorithm for automatic detection of blue shifted jets in the MOSES He II data, and has identified about 100. Jacob Plovanic is investigating the importance of 3D geometry in the formation of He II emission (Plovanic & Kankelborg(2012)). Shane Atwood has developed a code to remove the effects of disparate point spread functions in the three MOSES channels (Atwood & Kankelborg(2013)).

Graduate student J. Lewis Fox completed his PhD dissertation in 2011 based on MOSES data (Fox(2011)). He is now working at NSO Sac Peak on the Prominence Magnetometer instrument.

Much of the engineering work for the MSU rocket program has been done by undergraduate students. A number of these students have kept in touch with us after graduation. All those who have kept in touch with us are working productively in STEM fields. They include a mechanical engineer at a high tech startup, a physics PhD student at a large Midwest school, the founder of a specialty design and prototyping business, and a technical project manager at the Naval Undersea Warfare Center.

## 4 Relevance to NASA Objectives and Programs

The proposed observations and data analysis directly address NASA’s heliophysics science goal to “Understand the Sun and its interactions with the Earth and the solar system,” and the related science question “What causes the Sun to vary?” In particular, we hope to uncover the physics of the reconnection process in explosive events that have been observed by other NASA missions and instruments as cited in section 1. We will also look for signatures of mass and energy flow through the transition region. This addresses NASA’s objective to “understand the fundamental physical processes of the space environment from the Sun to Earth....”

A major goal of the Low Cost Access to Space program (LCAS) has always been “...testing new concepts in experimental techniques that may ultimately find application in free-flying Sun-Solar System Connection space missions.” The *MOSES* instrument, scheduled for its second flight in 2014, is unique among space instrumentation: an EUV imager that simultaneously provides doppler shift and linewidth information, and separates the intensities of multiple spectral lines that contribute to an image. *ESIS*, which will fly in tandem with *MOSES*, builds on that experience. *ESIS* is a smaller, lighter, more sensitive, and better performing embodiment of the concept behind *MOSES*. *ESIS* is a logical precursor to an explorer-class mission or mission of opportunity.

As emphasized in our coordinated observation plan (section 2.3), the *MOSES* and *ESIS* instruments provide totally unique capabilities, yet they have strong synergy with *SDO/AIA* and *IRIS*.

Finally, NASA has a longstanding interest in workforce development. The educational value of the *MOSES* program is well established (section 3.2).

## 5 Plan of Work

The proposed effort comprises four main parts:

1. Fly the reconfigured 46.5 nm MOSES-II instrument.
2. Analyze and publish results of the MOSES-II flight
3. Develop the new 63 nm ESIS instrument.
4. Fly ESIS in tandem with MOSES.
5. Begin analyzing data from the ESIS-MOSES flight.

These elements are layed out in the program schedule, figure 13. Of these, the first two items entailing work on MOSES-II, including all major procurements and salaries through about March 2013, are funded in part by previous awards, including a partial award from the previous LCAS round. Our budget details describe what is required to bring MOSES-II to flight. The development and flight of ESIS comprises the bulk of our proposal in terms of effort and cost.

The major long lead procurement for this rocket mission is the diffraction grating, which will be manufactured by Horiba Jobin-Yvon. We worked successfully with Horiba to procure and test the diffraction gratings for the successful NASA *IRIS* mission, and Horiba has recently delivered gratings for the upcoming MOSES-II flight. Horiba has quoted custom gratings for ESIS, and we have scheduled conservatively for their development.

We will continue to develop and extend the techniques of parallax and inversion developed during our experience with MOSES data (§ 2.4) throughout the performance period, applying them first to MOSES itself and then to ESIS when it is launched.

### 5.1 Roles & Responsibilities

The PI, Dr. Charles Kankelborg, takes overall responsibility for the completion of this project, dissemination of results, and technical reporting. Mr. Larry Springer will provide project management, scheduling, tracking finances, and holding the PI and team accountable. The two teams at MSU and MSFC will be in regular contact via teleconference, and will hold a sufficient number of face- to-face meetings to ensure a smooth and efficient development and integration of the ESIS instrument.

The MSU team will design, specify and procure the ESIS optics; design and fabricate optomechanics; integrate the ESIS electronics with the experiment section; perform calibrations and functional tests; and support integration and test at the range. MSU will send personnel to MSFC to participate in electronics testing and to become proficient in the operation of the ESIS electronics via MSFC-supplied EGSE. MSU is also responsible for all upgrades, testing, calibration, and operations of the existing MOSES instrument, such as repackaging and/or recabling of existing electronics to accommodate ESIS. Our student team and their current activities are described in section 3.2.

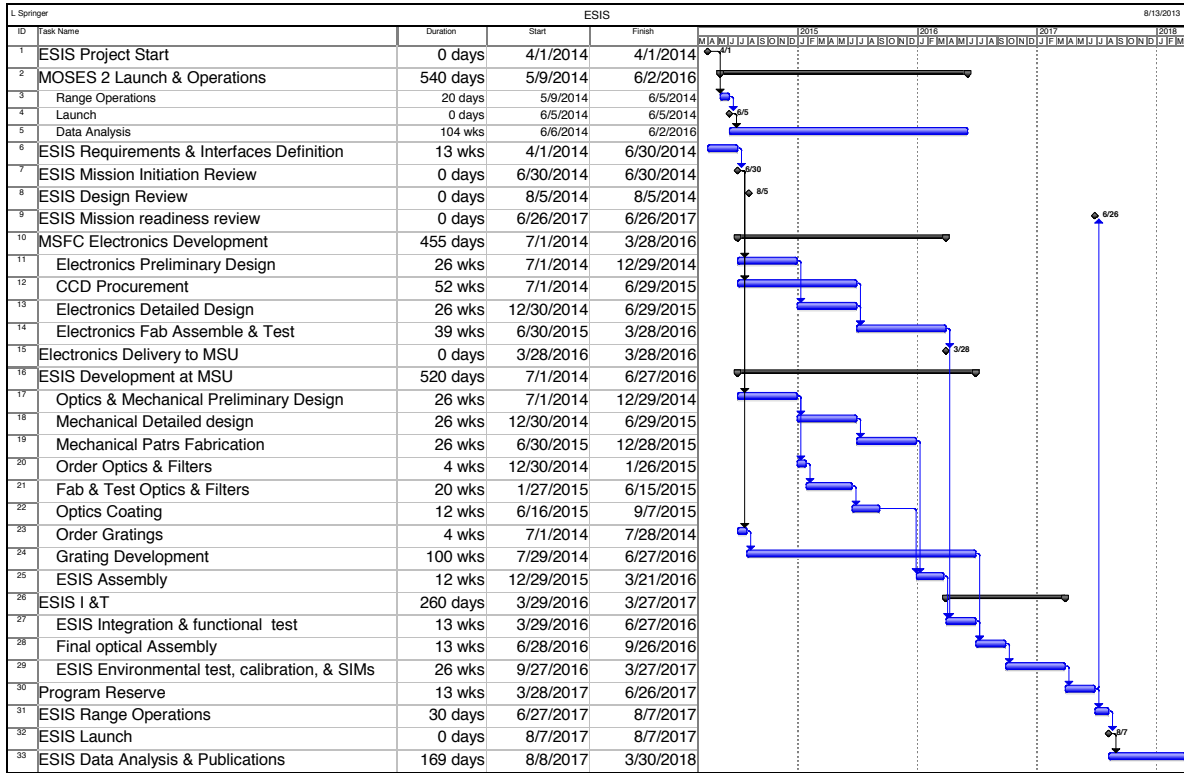


Figure 13: MOSES/ESIS schedule.

Co-Investigator Dr. Jonathan Cirtain will lead the contributions of MSFC. PM at MSFC is Mr. Todd Holloway. Co-Investigator Dr. Amy Winebarger will provide science support on camera development, ensuring that the cameras are tested to meet instrument requirements. The MSFC team takes responsibility for the ESIS camera electronics, control computer, software, telemetry interface, and will procure CCD sensors from E2V for the ESIS instrument. MSFC will provide permanent EGSE for ESIS, as well as training to MSU personnel and a few short support trips to MSU and to the range. Drs. Cirtain and Winebarger will also support the scientific data analysis, working with the MSU team including students.

## References

- Asai, A., Yokoyama, T., Shimojo, M., Masuda, S., Kurokawa, H., & Shibata, K. 2004, *The Astrophysical Journal*, 611, 557
- Atwood, S. & Kankelborg, C. 2013, in *AAS/Solar Physics Division Meeting*, Vol. 44, AAS/Solar Physics Division Meeting, 96
- Bárta, M., Vršnak, B., & Karlický, M. 2008, *A&A*, 477, 649
- Bhattacharjee, A., Huang, Y.-M., Yang, H., & Rogers, B. 2009, *Physics of Plasmas*, 16, 112102
- Courrier, H. & Kankelborg, C. 2013, in *AAS/Solar Physics Division Meeting*, Vol. 44, AAS/Solar Physics Division Meeting, 94
- Curdt, W. & Tian, H. 2011, *A&A*, 532, L9
- Curdt, W., Tian, H., & Kamio, S. 2012, *Sol. Phys.*, 280, 417
- Dere, K. P., Bartoe, J., Brueckner, G. E., Ewing, J., & Lund, P. 1991, *J. Geophys. Res.*, 96, 9399
- Doyle, J. G., Banerjee, D., & Perez, M. E. 1998, *Sol. Phys.*, 181, 91
- Feldman, U. 1987, *Atlas of extreme ultraviolet spectroheliograms from 170 to 625 Å. Volume 1; Volume 2*
- Fox, J. L. 2011, PhD thesis, Montana State University
- Fox, J. L. & Kankelborg, C. C. 2012, In preparation for *ApJ*
- Fox, J. L., Kankelborg, C. C., & Metcalf, T. R. 2003, in *Presented at the Society of Photo-Optical Instrumentation Engineers (SPIE) Conference*, Vol. 5157, *Society of Photo-Optical Instrumentation Engineers (SPIE) Conference Series*, ed. A. M. Larar, J. A. Shaw, & Z. Sun, 124–132
- Fox, J. L., Kankelborg, C. C., & Thomas, R. J. 2010, *ApJ*, 719, 1132
- Fox, L. & Kankelborg, C. C. 2009, in *AAS/Solar Physics Division Meeting*, Vol. 40, AAS/Solar Physics Division Meeting #40, 33.04–+
- Furth, H. P., Killeen, J., & Rosenbluth, M. N. 1963, *Physics of Fluids*, 6, 459
- Gontikakis, C. & Winebarger, A. R. 2012, in *10th Hellenic Astronomical Conference*, ed. I. Papadakis & A. Anastasiadis, 11–11
- Hahn, M., Landi, E., & Savin, D. W. 2012, *The Astrophysical Journal*, 753, 36
- Hahn, M. & Savin, D. W. 2013, *ArXiv e-prints*
- Harrison, R. A., Kent, B. J., Sawyer, E. C., Hollandt, J., Kuhne, M., Paustian, W., Wende, B., & Huber, M. C. E. 1996, *Metrologia*, 32, 647
- Innes, D. E., Inhester, B., Axford, W. I., & Wilhelm, K. 1997a, *Nature*, 386, 811



- Innes, D. E., Inhester, B., Axford, W. I., & Willhelm, K. 1997b, *Nature*, 386, 811
- Innes, D. E. & Teriaca, L. 2013, *Sol. Phys.*, 282, 453
- Kak, A. C. & Slaney, M. 1988, *Principles of computerized tomographic imaging*, Vol. 33 (Siam)
- Kankelborg, C. C. & Fox, J. L. 2004, in *Bulletin of the American Astronomical Society*, Vol. 36, American Astronomical Society Meeting Abstracts #204, 794–+
- Kankelborg, C. C. & Thomas, R. J. 2001, in *Proc. SPIE Vol. 4498*, p. 16–26, *UV/EUV and Visible Space Instrumentation for Astronomy and Solar Physics*, Oswald H. Siegmund; Silvano Fineschi; Mark A. Gummin; Eds., 16–26
- Lemen, J. R., Title, A. M., Akin, D. J., Boerner, P. F., Chou, C., Drake, J. F., Duncan, D. W., Edwards, C. G., Friedlaender, F. M., Heyman, G. F., Hurlburt, N. E., Katz, N. L., Kushner, G. D., Levay, M., Lindgren, R. W., Mathur, D. P., McFeaters, E. L., Mitchell, S., Rehse, R. A., Schrijver, C. J., Springer, L. A., Stern, R. A., Tarbell, T. D., Wuelser, J.-P., Wolfson, C. J., Yanari, C., Bookbinder, J. A., Cheimets, P. N., Caldwell, D., Deluca, E. E., Gates, R., Golub, L., Park, S., Podgorski, W. A., Bush, R. I., Scherrer, P. H., Gummin, M. A., Smith, P., Auker, G., Jerram, P., Pool, P., Souffi, R., Windt, D. L., Beardsley, S., Clapp, M., Lang, J., & Waltham, N. 2012, *Sol. Phys.*, 275, 17
- Masuda, S. 1994, *Nature*, 371, 495
- McKenzie, D. 2000, *Solar Physics*, 195, 381
- . 2013, *The Astrophysical Journal*, 766, 39
- Miklenic, C., Veronig, A., Vrsnak, B., & Hanslmeier, A. 2007, *A&A*, 461, 697
- Moses, D., Cook, J. W., Bartoe, J.-D. F., Brueckner, G. E., Dere, K. P., Webb, D. F., Davis, J. M., Harvey, J. W., Recely, F., Martin, S. F., & Zirin, H. 1994, *ApJ*, 430, 913
- Muglach, K. 2008, *ApJ*, 687, 1398
- Ohyama, M. & Shibata, K. 1998, *The Astrophysical Journal*, 499, 934
- Okamoto, T. & Yamaguchi, I. 1991, *Optics Letters*, 16, 1277
- Plovanic, J. & Kankelborg, C. C. 2012, in *American Astronomical Society Meeting Abstracts*, Vol. 220, American Astronomical Society Meeting Abstracts #220, 203.08
- Poletto, L. & Thomas, R. J. 2004, *Applied optics*, 43, 2029
- Qiu, J., Wang, H., Cheng, C., & Gary, D. E. 2004, *The Astrophysical Journal*, 604, 900
- Savage, S. L., McKenzie, D. E., & Reeves, K. K. 2012, *The Astrophysical Journal Letters*, 747, L40
- Savage, S. L., McKenzie, D. E., Reeves, K. K., Forbes, T. G., & Longcope, D. W. 2010, *The Astrophysical Journal*, 722, 329

- Shibata, K. c., Masuda, S., Shimojo, M., Hara, H., Yokoyama, T., Tsuneta, S., Kosugi, T., & Ogawara, Y. 1995, *The Astrophysical Journal Letters*, 451, L83
- Takasao, S., Asai, A., Isobe, H., & Shibata, K. 2012, *ApJ*, 745, L6
- Tousey, R., Bartoe, J.-D. F., Brueckner, G. E., & Purcell, J. D. 1977, *Appl. Opt.*, 16, 870
- Vernazza, J. E. & Reeves, E. M. 1978, *ApJS*, 37, 485
- Welsch, B., Abbett, W., DeRosa, M., Fisher, G., Georgoulis, M., Kusano, K., Longcope, D., Ravindra, B., & Schuck, P. 2007, *The Astrophysical Journal*, 670, 1434
- Windt, D. L., Bellotti, J. A., Kojrnattanawanich, B., & Seely, J. F. 2009, *Applied optics*, 48, 5502